Cell Coverage Analysis of 28 GHz Millimeter Wave in Urban Microcell Environment Using 3-D Ray Tracing

Jae-Hyun Lee[ID], Jeong-Sik Choi[ID], and Seong-Cheol Kim, *Senior Member, IEEE*

Abstract—In this paper, the channel characteristics and cell coverage of the 28 GHz millimeter wave (mmWave) band outdoors are investigated by developing an efficient 3-D ray-tracing simulation. First, the accuracy of the simulation is verified by comparing its results with actual measurements. The path loss (PL) agrees well in both line-of-sight (LOS) and non-LOS (NLOS) regions, whereas the shadowing factor exhibits differences in the NLOS regions. Additional simulations are conducted for downtown Gangnam, a representative high-rise urban area in Seoul, South Korea. The simulated and measured coverages of 300 base stations operating in 900 MHz long-term evolution band are compared and analyzed. For the LOS regions, PL of 28 GHz is 30 dB higher because of the free-space PL gaps, whereas PL varied in the NLOS regions because of multipath fading. In addition, the outage probability is determined to evaluate the validity of mmWave cell deployment and coverage for high-rise urban microcell environments. The contributions of this paper include LOS and outage probability models with low root-mean-square errors, indicating improvement over previously developed models.

Index Terms—Electromagnetic propagation, millimeter wave (mmWave) radio propagation, radio propagation, ray tracing.

I. INTRODUCTION

ACCORDING to the global mobile data traffic forecast by Cisco, the gross amount of mobile data traffic is expected to increase to 49 exabytes per month by 2021, which is seven times greater than the amount of traffic in 2016 [1]. Because of the unprecedented surge in mobile data usage, mobile network operators (MNOs) are currently encountering an explosive demand for data traffic. Because the current fourth-generation (4G) systems have already achieved spectral efficiencies close to the theoretical limit, utilization of a millimeter wave (mmWave) frequency band, to obtain more

bandwidth, is considered to be one of the most promising technologies for the development of fifth-generation (5G) wireless systems [2].

Among the potential mmWave bands, the 28 GHz band is considered, to be practical, for use in the 5G cellular network systems [3]–[5]. To ensure the success of such systems, a precise study of the radio propagation channel should be performed before the cell deployment. One way to evaluate the channel characteristics in a particular area is to measure the channel impulse responses at various receiver (Rx) locations within the target area. For this reason, the mmWave propagation channel has been investigated from several urban areas, such as Manhattan, NY, USA and Daejeon, South Korea [6]–[8]. However, the ability to obtain measurements in outdoor propagation environments is limited because the field measurements are often site-specific and time consuming.

Ray-tracing simulations, on the other hand, are widely adopted to model indoor and outdoor radio channels, alleviating the burden of extensive field measurement campaigns [9]–[11]. In a ray-tracing simulation, the electromagnetic wave that radiates from the base station is considered to be a bunch of rays using a ray-optic approximation, so a geometric solution is obtained based on the uniform theory of diffraction and geometric optics. In addition, the ray-optic approximation method well describes the short-wavelength electromagnetic wave propagation, so ray-tracing simulations can be effectively applied to the mmWave band. Therefore, ray-tracing simulations can provide geometrical channel impulse responses immediately, without requiring time-consuming measurement campaigns, when the geometric features are precisely modeled.

The problem is that the ray-tracing accuracy strongly depends on several features, such as the modeling accuracy of building structures, incremental angular steps of radiating rays, and rendering of scattering objects, including trees, cars, and people. In addition, wave propagation phenomena, such as reflection, diffraction, penetration, and scattering, should be modeled precisely. Efficient algorithms were developed for 3-D ray tracing in several early studies [10]. However, because most ray-tracing simulation tools and related publications lack detailed information about the simulation environment, the ray-tracing simulators for urban microcell environments are very limited. For example, in [6], [12], and [13], ray-tracing tools were used to model 28 GHz channels; however,

simulation parameters, such as the maximum numbers of reflections, penetrations, and diffractions, were not thoroughly investigated through comparison with measurements.

In this paper, instead of simply using the commercial ray-tracing simulation tool, a new ray-tracing simulation tool based on the vertical-plane-launch (VPL) method was developed to analyze the mmWave communication coverage in an urban microcell environment [14]. The novelty of our research is twofold. First, parametric values enabling realistic simulation of the urban microcell environment were identified. Our simulator is designed to calculate vertical and horizontal diffractions, which are important when simulating outdoor wireless channels, and the simulation accuracy was verified by the comparison of the results with actual measurements obtained in the urban microcell environment of Daejeon, South Korea. We also found that vertical and horizontal diffractions over buildings significantly enhanced the number of multipaths in this high-rise urban district.

Next, extensive simulations were conducted to estimate the characteristics of the 28 GHz mmWave band channel in a high-rise urban environment for various transmitter (Tx) and Rx positions. We used actual base station locations operated by MNOs in Gangnam district to investigate the feasibility of similar long-term evolution (LTE) base station deployment. To do so, the coverages of the 900 MHz LTE and 28 GHz mmWave bands by various base stations were compared. In addition, line-of-sight (LOS) and outage probabilities were determined to identify the coverage of the 28 GHz mmWave channel for both LOS and non-LOS (NLOS) regions.

The rest of this paper is organized as follows. The VPL method and wave propagation models are described in Section II. The comparison of simulation results with measurements obtained by the Electronics and Telecommunication Research Institute (ETRI), South Korea, is presented in Section III. In this paper, measurements were conducted for the central district of Daejeon, South Korea. The associated discussion and ray-tracing results from the Gangnam district are provided in Section IV. Because Gangnam is one of the most thriving areas in South Korea and consists of dense high-rise buildings, the coverage analysis of the 28 GHz band is expected to help the MNOs facilitate the 28 GHz mmWave cellular network in high-rise urban environments.

II. PROPAGATION MODELING IN RAY-TRACING SIMULATION

A. VPL Method

The VPL method was originally proposed in 1998 by Liang and Bertoni [14] to simulate the 3-D radio propagation channel. We developed a ray-tracing simulator using C++ code following the physical concepts of the VPL method by dividing the simulation space into vertical and horizontal planes. Unlike the general 3-D ray shoot-and-bounce method that generates rays for all azimuth and elevation angles [10], the VPL method separates the propagation domain into horizontal (rooftop) and vertical (lateral) planes. First, rays are launched in the horizontal direction, which is similar to the existing 2-D pincushion method, as shown in Fig. 1. Rays at this stage represent the vertical planes that contain all of
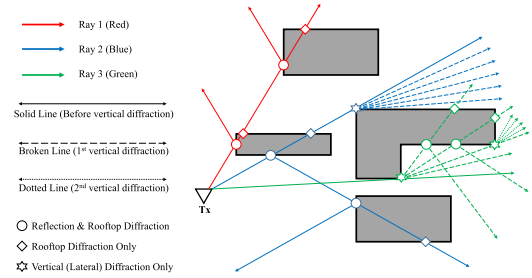

Fig. 1.   Rays generated in the horizontal plane using the VPL method.

the elevation angles at which rays are launched from the source point. When the vertical plane hits the wall, it is divided into two planes—one that passes over the building wall and another that is reflected in the direction of specular reflection. The vertical plane that continues in the incident direction contains the rays that propagate directly over the building or are diffracted over the building at its horizontal edge (roof). The other vertical plane contains rays that have been specularly reflected from the building walls.

After considering the propagation of the rays (vertical planes) in the horizontal domain, the path between Tx and Rx is calculated in the vertical domain. Vertical plane segments can reach Rx when Rx is in the vertical wedge of the ray and within the Rx capture circle. The vertical wedge is the hyperplane that remains against the wall. Using the vertical wedge concept, the regions that cannot be reached from the horizontal rays are readily excluded, thereby reducing the computing redundancy. If it is determined that a ray reaches Rx, the unfolded path from Tx to Rx is calculated and all of the reflection and diffraction coefficients of each ray segment are calculated and recorded. The methods used to calculate the reflection and diffraction coefficients are described in Sections II-B and II-C.

Along with the VPL algorithm, we adopted two methods to reduce the computation time: 1) the binary space partitioning (BSP) algorithm and 2) the quad-tree method. We applied the BSP algorithm [15] to enable the wall intersection to be found faster than it could using the existing brute-force search algorithm. Before tracing ray paths, our simulator reads all of the vertical wall data, divides the simulation space into partial spaces, and saves the space information in a binary tree structure, as shown in Fig. 2. By employing this procedure, the walls that are irrelevant to a ray that radiates in a certain direction can be excluded efficiently from the intersection calculation. In urban microcell environments, it is important to reduce the calculations because of the vast amount of building wall data. The quad-tree method is relevant to the positions of the Rx points. A quad-tree is a tree data structure and can be used to partition a 2-D space by recursively subdividing it into four quadrants. Along with the BSP algorithm, the quad-tree algorithm speeds up the search for paths to the Rx points.

B. Reflection

Assuming that the dimensions of the impinging wall are large compared with the wavelength of the electromagnetic
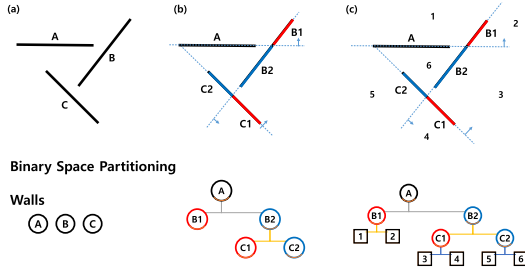
Fig. 2. Example of BSP algorithm. (a) Three walls are located. (b) Wall B is divided into segments (B1 and B2) by the line extending from wall A. Wall C is also divided into segments (C1 and C2) by the line extending from wall B2. (c) Using the BSP algorithm, 2-D planes are separated into six polygonal planes.

Fig. 3. Schematic of wedge diffraction.

wave and that the media is homogeneous, the reflection coefficients can be derived from the Fresnel equation [16]. According to the Fresnel equation, the reflection coefficients for both parallel and perpendicular polarizations, Γ_p and Γ_s, respectively, can be obtained using the wave impedance as follows:

$$\Gamma_s = \left| \frac{Z_2 \cos\theta_i - Z_1 \cos\theta_t}{Z_2 \cos\theta_i + Z_1 \cos\theta_t} \right|^2 \tag{1}$$

$$\Gamma_p = \left| \frac{Z_2 \cos\theta_t - Z_1 \cos\theta_i}{Z_2 \cos\theta_t + Z_1 \cos\theta_i} \right|^2 \tag{2}$$

where Z_1 and Z_2 are the wave impedances of media 1 and 2, respectively, and θ_i and θ_t are the incident and refracted angles, respectively. The wave impedance is dependent on the relative permittivity ϵ_r of the walls, and the permeability is μ_0 for both air and nonmagnetic media used for the building materials. The conductivity σ is assumed to be negligible for nonconducting building materials, such as brick, glass, and concrete. In addition, using Snell's law, the refracted angle can be substituted with the equation involving the incident angle and refractive indices of the media, enabling the above-mentioned reflection coefficients to be expressed as

$$\Gamma_s = \left| \frac{\cos\theta_i - \sqrt{\epsilon_r - \sin^2\theta_i}}{\cos\theta_i + \sqrt{\epsilon_r - \sin^2\theta_i}} \right| \tag{3}$$

$$\Gamma_p = \left| \frac{\epsilon_r \cos\theta_i - \sqrt{\epsilon_r - \sin^2\theta_i}}{\epsilon_r \cos\theta_i + \sqrt{\epsilon_r - \sin^2\theta_i}} \right|. \tag{4}$$

From (3) and (4), the reflection coefficient can be determined by two parameters: θ_i of the ray and ϵ_r of the wall.

ϵ_r depends on the frequency of the radio waves and the intrinsic properties of the medium. However, for the 28 GHz band, it is difficult to obtain the nominal value of the relative permittivity of the building materials for the ray-tracing method. In [14], ϵ_r was set to 6 for carrier frequencies of 900 and 1900 MHz. In a recent paper [17], ϵ_r spectra for some building materials were reported; however, the 28 GHz band was not included. In addition to frequency dependence, building materials are important because ϵ_r changes considerably according to the building material. For example, glass has ϵ_r values ranging from 6.08 at 5 GHz to 8.9 at 62.4 GHz, whereas brick has ϵ_r values ranging from 4.5 at 2 GHz to 3.95 at 60 GHz. Recently, Samsung Electronics reported ray-tracing simulation results for the 28 GHz band assuming
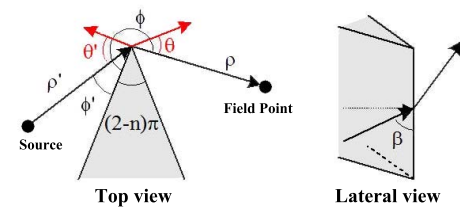
that all buildings are made of concrete, with $\epsilon_r = 6.5$ and $\sigma = 0.668$ S/m at 28 GHz [18]. In our simulation, ϵ_r was set to values ranging from 6 to 8 according to the building exterior type [18]–[20].

C. Diffraction

Both the vertical and horizontal diffraction coefficients can be obtained using the wedge diffraction model [21]. Although the power of diffracted rays is significantly less than that of the incident ray, diffraction is important for wireless communication because it enables wireless signal to reach shadowed regions. However, it is difficult to model diffraction in ray-tracing simulations because all of the edges and vertices of objects become secondary source points that generate numerous diffracted rays, which increase the calculation complexity. To manage this problem, modified Luebber's formulation is utilized to calculate the diffraction coefficient [21], [22]. Based on the geometric theory of diffraction [23], the electric field E_{GTD} at a field point can be expressed as follows:

$$E_{\text{GTD}} = E_0 \frac{e^{-jk\rho'}}{\rho'} D_\parallel^\perp \sqrt{\frac{\rho'}{\rho(\rho' + \rho)}} e^{-jk\rho} \tag{5}$$

where E_0 is the source amplitude; k is the wavenumber; ρ and ρ' are the distances between the source and diffraction edge and between the diffraction edge and field point, respectively; and $D_\parallel^\perp$ represents the diffraction coefficients that depend on the polarization of the incident field on the edge. For a nonconducting wedge, the diffraction coefficients for each polarization can be calculated using

$$D_\parallel^\perp = \frac{-e^{-j(k(\rho+\rho')+\pi/4)}}{2n\sqrt{2\pi k}\sin\beta}$$
$$\times \left\{ \frac{F(kLa^+(\phi-\phi'))}{\tan[(\pi+\phi-\phi')/2n]} + \frac{F(kLa^-(\phi-\phi'))}{\tan[(\pi+\phi-\phi')/2n]} \right.$$
$$\left. + \Gamma_{0\parallel}^\perp \frac{F(kLa^-(\phi+\phi'))}{\tan[(\pi+\phi-\phi')/2n]} + \Gamma_{n\parallel}^\perp \frac{F(kLa^+(\phi+\phi'))}{\tan[(\pi+\phi+\phi')/2n]} \right\} \tag{6}$$

where $\Gamma_{0\parallel}^\perp$ and $\Gamma_{n\parallel}^\perp$ are the reflection coefficients for either perpendicular or parallel polarization for the front wall surface with incident angle ϕ' and the backward wall with reflection angle $n\pi - \phi$, respectively; $F(x) = 2j\sqrt{x}e^{jx}\int_{\sqrt{x}}^\infty e^{-j\tau^2} d\tau$ is a Fresnel integral; $L = (\rho\rho'/(\rho + \rho'))$; $a^\pm(\beta) = 2\cos^2[(2n\pi N^\pm - \beta)/2]$; $\beta = \phi \pm \phi'$; and $N^\pm$ are the integers that most nearly satisfy the equation $2\pi n N^+ - (\beta) = \pi$ or $2\pi n N^- - (\beta) = -\pi$ [21]. Fig. 3 shows the schematic of wedge diffraction and the variables explained earlier.
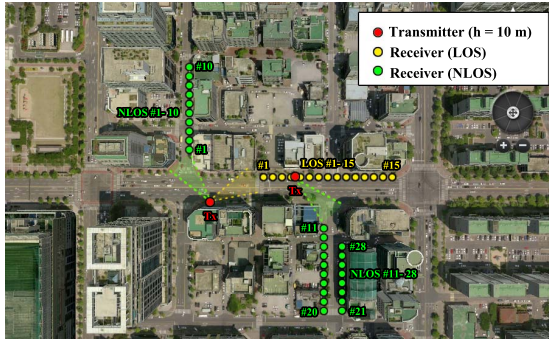
Fig. 4. Measurement points and Tx points in Daejeon. The yellow and green circles indicate the LOS and NLOS Rx points, respectively, that were used to obtain the measurements reported in [19].

The simulator was designed to calculate up to two lateral (vertical) diffractions for a single ray path. This limitation cause diffraction loss identical to that reported in [24] for the 28 GHz band. Thus, rays that are laterally diffracted more than or exactly three times are excluded from the path loss (PL) calculations because these rays have insignificant magnitudes.

III. VALIDATION OF RAY-TRACING SIMULATION

A. Measurement Campaign in and Simulation of Daejeon

To verify the performance of the ray-tracing simulator, the simulation results were compared with the actual mmWave channel measurements. Park *et al.* [19] reported 28 GHz mmWave channel measurements obtained using the ETRI mmWave band exploration and channel sounder. The channel sounder has a dynamic PL range extending up to 170 dB with a 500 MHz bandwidth at 28 GHz. The directional antenna for Tx has a half-power beamwidth (HPBW) of 30° and a main lobe gain of 15.4 dBi at a height of 10 m, corresponding to below-rooftop scenarios. An omni-directional antenna with 5 dBi gain and a directional horn antenna[1] with 10° HPBW and 15.4 dBi gain were used for Rx at 1.5 m above ground (pedestrian level) to collect data. The Rx antenna rotated 360° horizontally in 10° steps, and the elevation angle was fixed at 0°. The channel measurements were performed in the urban district of Daejeon, South Korea, as shown in Fig. 4. The measurement site was a typical urban microcell environment composed of 7–11 story buildings (20–35 m high) with 24–35 m wide streets between buildings, as explained in [19].

To simulate the mmWave channel in the same area, we obtained the geographic information system (GIS) data in the ESRI shapefile format from the Spatial Information Industry Promotion Institute, an organization affiliated with the Ministry of Land, Infrastructure and Transport, South Korea. The ESRI shapefile format is a geospatial vector data format widely used for GIS and industrial software. The building data encompass various 3-D information, such as the coordinates of complex polygonal structures and the multiple

TABLE I
ROOT-MEAN-SQUARE ERROR OF SIMULATION DATA

RMSE	R=1 D=0	R=2 D=0	R=3 D=0	R=4 D=0	R=5 D=0	R=6 D=0	R=6 D=1	R=6 D=2
LOS	1.68	1.69	1.69	1.69	1.69	1.69	1.66	1.66
NLOS	40.21	33.67	21.79	6.08	6.00	6.00	5.62	5.27
Total	28.46	23.84	15.46	4.46	4.41	4.41	4.14	3.91

heights of buildings based on an absolute elevation; however, the shapefile does not contain small obstructions such as trees, cars, and lamp posts. Detailed GIS data, such as exact coordinates, absolute altitudes, and numbers of building stories in urban areas, were obtained by parsing the shapefiles.

B. Parametric Value for Ray Tracing

Fig. 4 shows the Rx locations measured by ETRI. The root-mean-square error (RMSE) values for overall LOS and NLOS points were arranged in Table I. For LOS regions, the RMSE values were similar because the dominant direct path exists for each LOS point. For NLOS regions, however, the RMSE value decreased as more reflected and diffracted signals were included. The impact of the maximum number of reflection (R) was saturated when it becomes 5 to 6. Although the amount of computation is increased, but R has been set to 6, taking into account the Rx point far from the measuring point. The change in RMSE due to the maximum number of diffraction (D) was not remarkable, but the RMSE of NLOS decreases from 6.00 to 5.27.

As shown in Fig. 5, the simulation results of specific points are also the closest to the measured results when R and D are six and two, respectively. As R increases, the number of paths reaching the Rx position increases, so the magnitude of the PL gradually decreases. Also, the results for NLOS locations #5 and #8 indicate that as D increases, the magnitude of the received signal component increases further; thus, the PL decreases due to the diffracted received signals. The maximum number of horizontal diffractions was also set to four to consider rooftop diffraction.

The slight difference between the average PL and simulation results for six reflections and two vertical diffractions (orange bar) is due to the measurement limit. A Tx antenna with a fixed elevation angle and a rotating Rx antenna were employed to obtain the measurements; however, omni-directional incident rays at the both the Tx and Rx antennas were considered in the simulation. Note that, the PL results in Figs. 5 and 6 exclude the Tx and Rx antenna gains, so they represent the signal attenuation of 28 GHz propagation channel between Tx and Rx as a function of the propagation distance. In addition, transmitted and scattered rays are time-consuming to model and are very weak compared with reflected and diffracted rays [2], [4], [7], [8], so transmission and scattering were excluded from the ray-tracing model.

C. LOS Path Analysis

The scatter plots of the measured LOS and NLOS PLs are presented in Figs. 6(a) and (b), respectively. Including the measurement points, we evaluated the PLs for Rx locations
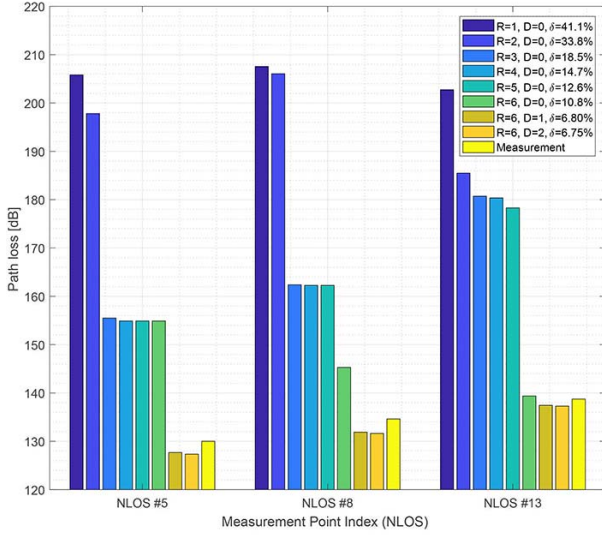
Fig. 5. Comparison of average measured PLs with those simulated for various maximum numbers of reflections and vertical diffractions [19]. Error rate δ represents the total percent error for all 28 NLOS points.

every 10 m along the grid lines. Among all 3721 of the Rx grid points around Tx in the center, those located inside the building were excluded; thus, 2400 street-level Rx points were simulated. For both the LOS and NLOS path analysis, the close-in free-space reference distance PL model [26] was used to compare the channel parameters and can be expressed as

$$PL(f, d)[\text{dB}] = \text{FSPL}(f, 1 \text{ m}) + 10n \log_{10} \frac{d}{1 \text{ [m]}} + X_\sigma \quad (7)$$

where n is the PL exponent (n), X_σ is a zero-mean Gaussian random variable with a standard deviation of σ in decibels, and FSPL is the free-space PL at the reference distance of 1 m, which is given by

$$\text{FSPL}(f, 1 \text{ m})[\text{dB}] = 20 \log_{10} \frac{4\pi f}{c} \quad (8)$$

where c is the speed of light.

At the LOS points, the n was 2.1 and 1.87 for the measurements and simulation, respectively. Thus, the n of the measurements is higher than that of the simulation results. This finding is reasonable because the ray-tracing model includes multipaths with high PLs, whereas they are excluded from actual measurements because multipaths corresponding to the received signals lower than the noise floor cannot be resolved. Furthermore, multipaths from sidelobe directions cannot reach the Rx point when a directional antenna is used; however, ray tracing includes all multipath components with powers as much as 30 dB lower than that of the strongest received signal.

From the n results, a waveguide effect caused by the urban buildings is evident. In addition, the simulation data that are far beyond the maximum distances in [19] (180 m for LOS and 140 m for NLOS) are incorporated, including the results obtained at the actual measurement points [shown in Fig. 6(c) as yellow stars]. The measurement results only included the dominant LOS signals; thus, σ was 1.8 dB.
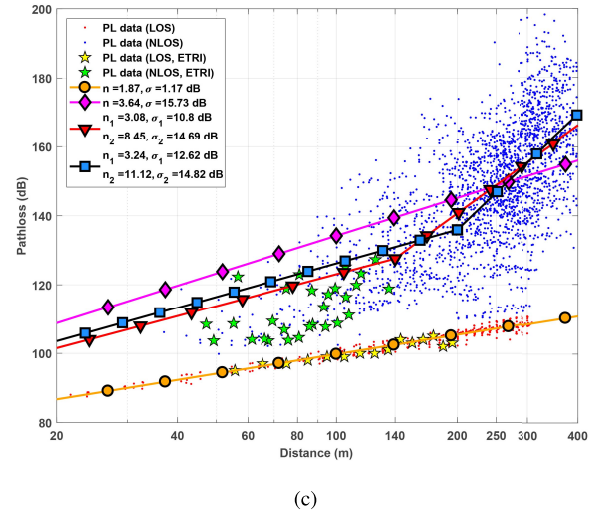

(a)

(b)

(c)
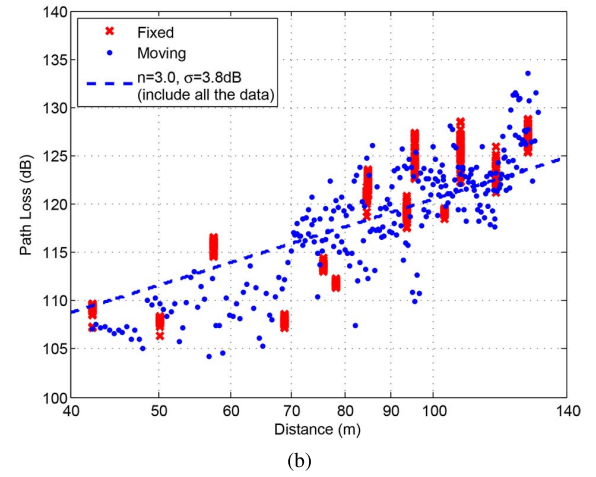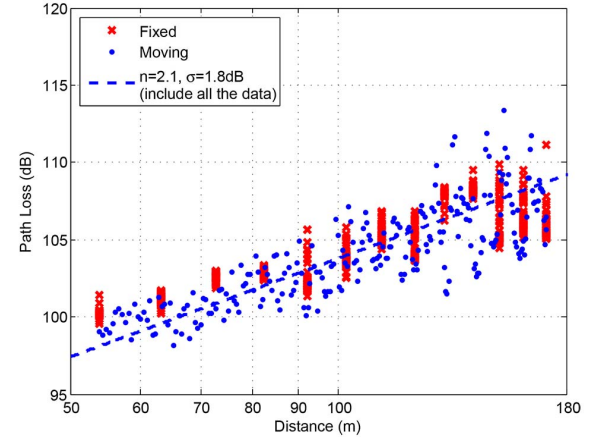
Fig. 6. LOS and NLOS PL results for Daejeon obtained by both measurement [19] and simulation. The simulation covered approximately 400 m, and the simulation results exhibit more scatter than the measurements. (a) 28 GHz LOS results of ETRI measurements. (b) 28 GHz NLOS results of ETRI measurements. (c) 28 GHz ray-tracing simulation results.

Because deterministic rays were used in ray tracing and the stochastic scattering effect was not modeled, σ is only 1.17 dB, which agrees well with the measurement results.

TABLE II
CHANNEL PARAMETERS FOR LOS AND NLOS

Models	LOS/ NLOS	d_{th} [m]	Observation Range [m]	PLE (n)	σ [dB]
Measurement	LOS	-	50–180	2.1	1.8
	NLOS	-	40–140	3.0	3.8
Simulation (Single-slope)	LOS	-	50–400	1.87	1.17
	NLOS	-	20–400	3.64	15.73
Simulation (Dual-slope)	NLOS	140	20–140	3.08	10.8
			140–400	8.45	14.69
Simulation (Dual-slope)	NLOS	200	20–200	3.24	12.62
			200–400	11.12	14.82

TABLE III
HIGH-RISE URBAN ENVIRONMENT SIMULATION DETAILS

Simulation Region	Downtown Gangnam, Seoul
Simulation Range	400 m for all directions
Number of Buildings	600–1200 (depending on Tx)
Number of Tx points	300
Height of Tx	10 m above ground
Number of Rx	2,500 (depending on Tx)
Spacing between Rx	10 m
Height of Rx	1.5 m above ground
Beam Spacing	0.1° in azimuth angle
Receivable Power Range	30 dB less than the strongest path
Max No. of Reflections	6
Max No. of V-Diffractions	2
Max No. of H-Diffractions	4

D. NLOS Path Analysis

In the NLOS regions, n values of 3.0 and 3.64 were obtained from the measurements and simulation, respectively. However, as shown in Fig. 6(c), the single-slope PL model does not fit the results for Tx–Rx distances less than 200 m; thus, the shadowing factor soars to 15.73 dB. This increase is attributable to the large quantities of Rx points extending to 400 m in both the single- and dual-slope PL models, whereas measurements were only obtained at 28 NLOS points that were locally correlated, as shown in Fig. 4. In the measurements, the Rx points were located in two adjacent areas and a directional antenna was used; therefore, the rays went through similar paths along Rx and moderate PL data were obtained. On the other hand, as shown in Fig. 6(c), the NLOS PL values range from approximately 100 to 200 dB.

The results indicate that the PL of an Rx point depends on the spatial environment around it. Even with the same Tx–Rx distance, the propagation characteristics, such as the numbers of reflections and diffractions, change severely depending on the location of Rx in the urban microcell environment. Early reports also stated that the PL of an NLOS region is highly site-specific [13], [26]. To model the NLOS regions more accurately, dual-slope models with the threshold distances d_{th} of 140–200 m were adopted in those studies. Following this method, we selected d_{th}s of 140 m (inverted red triangles) and 200 m (blue squares) for the NLOS PL model, and the results are presented in Fig. 6(c). The dual-slope PL model for the NLOS regions shows relatively low shadowing, and the n corresponding to distances less than 200 m are close to the measurement results (3.08 for $d_{\text{th}} = 140$ m and 3.24 for $d_{\text{th}} = 200$ m). The results are summarized in Table II.

The comparison between the simulation results and measurements and the distribution of the additional PL results in the NLOS and LOS regions in Daejeon district shown in Figs. 5 and 6(c) prove that our ray-tracing simulation is valid for evaluating the 28 GHz mmWave propagation channel. Finally, another representative urban district, downtown Gangnam, was modeled and simulated to analyze the usability of the 28 GHz mmWave propagation channel for cellular networks.

IV. ANALYSIS OF 28 GHZ MMWAVE PROPAGATION CHANNEL IN URBAN ENVIRONMENT

A. Downtown Gangnam Simulation Scenario

Using the ray-tracing simulation, the 28 GHz mmWave band radio channel was simulated in the downtown area of Gangnam, Seoul. Gangnam is one of the central commercial districts of Seoul, and it has a floating population of millions of people daily because it contains the head offices of major companies, numerous shopping centers, and underground subway transfer stations. Most buildings have five to ten stories and are more than 20 m high; thus, the site well represents an urban microcell environment. We obtained channel information for various urban microcell environments by performing computation for 300 Tx locations and integrated various channel information for the urban environments. The Tx locations were set to the positions where the actual current 4G cellular communication base stations operate. The simulation region was designed to include all of the buildings within 400 m of each Tx.

If the Rx area is equal to the building area in the simulation, some of the important multipaths reflected or diffracted from the buildings located further than 400 m would be missed. Therefore, the Rx area was set to extend 300 m from each Tx, and Rx points were created at 10 m intervals. Because the expected cell coverage radius for the 28 GHz mmWave band is widely recognized to be 200–300 m, we set the range for Rx points to be 100 m shorter than that of the simulated building regions. Since Rx should be at street level, we excluded the grid points that were on or inside the buildings. Regardless of the Tx locations, we computed more than 2500 Rx points and their PLs. These points covered all of the main streets, alleyways, and areas surrounded by high-rise buildings. Both the aerial view and plotted image of one of the simulation regions are shown in Fig. 7. The details of the simulation parameters are provided in Table III.

B. Coverage Comparison With 900 MHz LTE Band

First, ray-tracing simulations were conducted by changing the carrier frequency to compare the mmWave characteristics with those of the existing 900 MHz LTE band. Fig. 8 graphically depicts the PL differences between 900 MHz and 28 GHz. The FSPLs of the 28 GHz mmWave and 900 MHz LTE bands are 61.385 and 31.527 dB, respectively. Note that not only the ϵ_r, but also the variables, such as FSPL, Fresnel radius, reflection and diffraction coefficients, and wedge diffraction angles, were all affected by the frequency change [8], [14]. Because of the FSPL gap in the mmWave band, the PL of the 28 GHz band in the LOS regions is approximately 30 dB higher than that of the 900 MHz band. Fig. 9 shows the cumulative distribution functions (cdfs) for
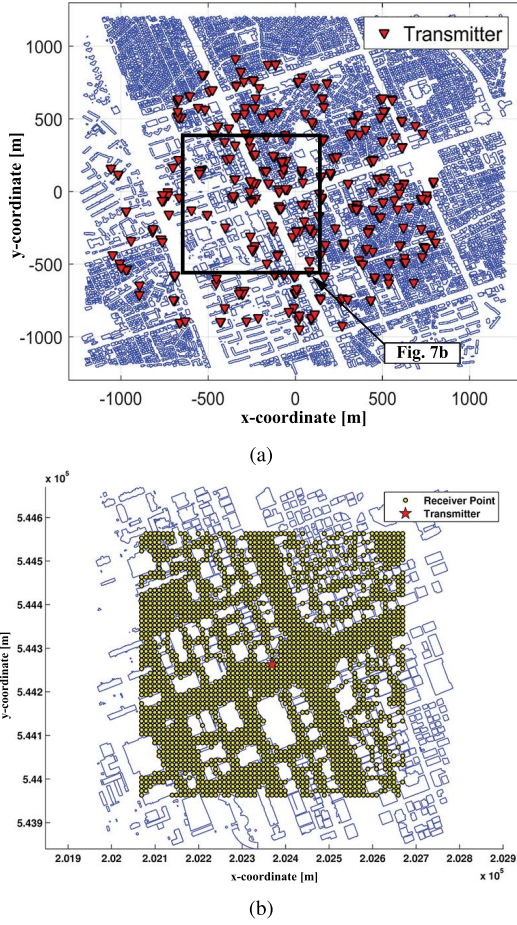
(a)

(b)

Fig. 7. Aerial view and plotted image of Gangnam district. The simulation region is about 800 m×800 m, and the Rx points are within 300 m×300 m based on the Tx location. (a) Aerial view of simulation region. (b) Plotted image of simulation region.

both the LOS and NLOS simulation results. These demonstrate that the PL in the LOS regions has gaps at certain values, while the PL in the NLOS regions changes because of the multi-path fading. Dense high-rise buildings in the northeast and northwest regions severely block the rays, causing the PLs in those areas to exceed 150 dB; meanwhile, the relatively sparse regions in the southwest and wide streets exhibit lower PLs.

In the LOS regions, the strongest LOS path dominates the received power; thus, the PL decrease is proportional to the distance in both spectra. In the NLOS regions, the reflection coefficients calculated for both frequencies are equal when the incident angles are equal because (3) and (4) only depend on the incident angle and ϵ_r. To compare the results corresponding to different reflection coefficients, ϵ_r should be modeled for each band separately based on the measured data, as noted in Section II. The diffraction coefficient is calculated differently because not only the early reflection coefficient, but also the wavenumber k is present in (6). Since the k depends on the carrier frequency, the PLs of the two bands differ in the region in which the dominant multipaths are diffracted rays.

C. Outage Probability in Omni-Directional Tx–Rx Distance

It is important to examine the outage probability to determine a reasonable coverage distance to ensure cellular network
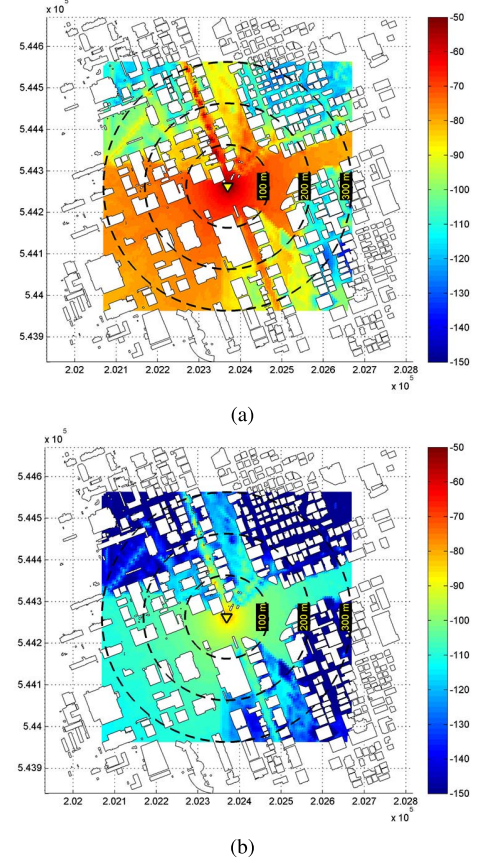

(a)

(b)

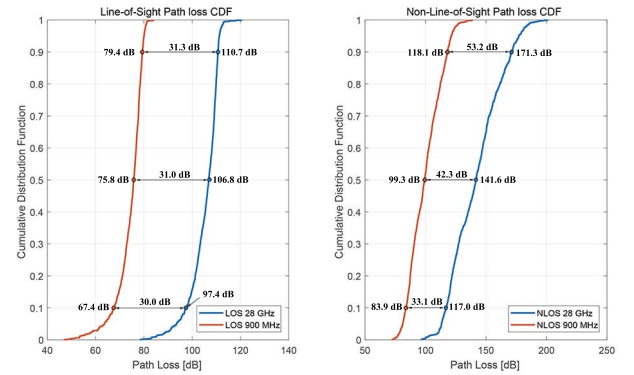Fig. 8. Comparison of (a) 900 MHz and (b) 28 GHz coverage.

Fig. 9. cdfs corresponding to 900 MHz and 28 GHz. The LOS position difference for each percentile is approximately equal to 30 dB, while this difference increases with the percentile in the NLOS results.

reliability. For the 28 GHz band, the outage probability was recently presented in [26] and [27]. In [27], 25 Rx locations and three Tx locations were considered, yielding 75 Tx–Rx pairs; on the other hand, more than 800 000 Tx–Rx pairs were simulated for 300 Tx locations in this paper, as shown in Fig. 7. For the MNO, whether the location of the current base station is applicable when installing the mmWave cell or whether to add a new base station location is an important criterion for mobile network operation [2].

Because of the intrinsic high FSPL in the mmWave band, the cell radius is expected to be less than that of the current LTE-band cells. Ongoing studies have indicated that a
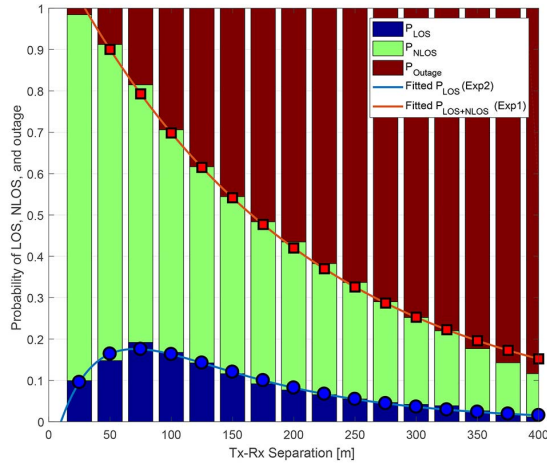
Fig. 10. Outage probabilities in Gangnam district for 28 GHz and Tx–Rx distances up to 400 m.

radius of 200 m is possible when mmWave-based wireless communication techniques, such as adaptive antennas, spatial beamforming, or massive multiple-input–multiple-output techniques, are utilized [28], [29]. Many researchers have stated that the maximum measurable PL of a system is approximately 160–180 dB, and set that to the outage value. However, the maximum measurable PL should be based on the channel measurement system. Accordingly, the received signal sensitivity is much higher than those of the commercial wireless devices. Several uplink and downlink budget examples were compared for LTE, high-speed packet access, and the global system for mobile communication in [30], and the maximum PL was about 160 dB. In our simulation, the maximum detectable PL was set to 150 dB considering the link budgets of mmWave systems; thus, Rx points with PL values higher than 150 dB were regarded as outage points.

In Fig. 10, the Rx points are divided into 25 m bins, and the LOS, NLOS, and outage point ratio are depicted as a stacked bar graph based on the overall number of Rx points for each bin. Unlike the results presented in [26] and [7], the LOS ratio remains constant for Tx–Rx distances greater than 200 m because the number of LOS points depends on the Tx location. This difference is attributable to the high-rise environment. The LOS and outage models described in [7] were based on measurements obtained at limited Tx and Rx positions in New York, whereas we simulated a diverse high-rise urban environment with actual base station locations using ray tracing. The reason for low LOS probability at a short distance is that some Rx points are classified as NLOS because the rooftop of the building interferes with the LOS path to the ground even if Tx is located on the building. In addition, since the minimum distance bin was set to 0–25 m, there exist NLOS points blocked by other buildings. However, these NLOS points receive sufficient signal strength from relatively short reflection and diffraction paths by the nearby terrain. Therefore, the cumulative probability of LOS and NLOS is approximately 1 at the nearest distance and decreases with increasing Tx–Rx distance. Because the number of Rx

TABLE IV
LOS, NLOS, AND OUTAGE PROBABILITIES OF URBAN ENVIRONMENTS

	Fitting Model	Coefficient	R^2	RMSE
$P_{\text{LOS}}(x)$	Exponential 2 $ae^{bx} + ce^{dx}$	$a = 0.4561$ $b = -0.008463$ $c = -0.556$ $d = -0.02836$	0.9821	0.008373
$P_{\text{LOS+NLOS}}(x)$	Exponential 1 ae^{bx}	$a = 1.161$ $b = -0.005083$	0.9955	0.01932
$P_{\text{Outage}}(x)$	$1 - P_{\text{LOS+NLOS}}$			

points is site-specific and local scatterers were not considered, the LOS, NLOS, and outage point numbers can vary; however, it was determined that the LOS and outage point ratios could be modeled with exponential functions. For the expected cell radius of 200 m, the outage points ratio is approximately 50%, and the probability function model is summarized in Table IV.

V. CONCLUSION

This paper presented the results of 3-D ray-tracing simulations of the 28 GHz mmWave band. This type of simulation requires tremendous computational overhead to account for the overall azimuth and elevation angles for the given simulation location. Using the VPL method, we separated the 3-D space into vertical and horizontal domains, which reduced the computational overheads without significant loss of paths between Tx and Rx.

To verify the accuracy of our simulation tool, the simulation results in Daejeon were compared with the measurements obtained by ETRI for the same site. Based on the comparison between the measurements and extensive simulation results, we suggested effective parametric values for the numbers of reflections and vertical and horizontal diffractions. Using the verified simulation tool, another simulation was conducted to investigate the feasibility of 28 GHz mmWave band using the current LTE-band base station locations in Gangnam, a representative high-rise urban environment in Seoul. Along with the extensive simulation results, single- and dual-slope PL models with different critical distances were summarized to enable PL modeling for the 28 GHz mmWave band.

Because of the high FSPL in the 28 GHz band, the results for the LOS regions exhibited constant PL differences of approximately 30 dB, whereas those for the NLOS regions varied because of multipath fading through reflection and diffraction. We suggested statistical models of the LOS, NLOS, and outage ratios containing various Tx–Rx pairs not included in previous studies, in which the measurements or simulation results were limited. The data presented in this paper are expected to facilitate studies on the development of 28 GHz mmWave cellular networks in urban microcell environments.

REFERENCES

[1] C. V. Forecast, "Cisco visual networking index: Global mobile data traffic forecast update, 2016–2021 white paper," Cisco Public Inf., San Jose, CA, USA, White Paper, vol. 1, pp. 1–35, 2017.

[2] T. S. Rappaport et al., "Millimeter wave mobile communications for 5G cellular: It will work!" IEEE Access, vol. 1, pp. 335–349, May 2013.

[3] A. I. Sulyman, A. T. Nassar, M. K. Samimi, G. R. MacCartney, Jr., T. S. Rappaport, and A. Alsanie, "Radio propagation path loss models for 5G cellular networks in the 28 GHz and 38 GHz millimeter-wave bands," IEEE Commun. Mag., vol. 52, no. 9, pp. 78–86, Sep. 2014.

[4] M. R. Akdeniz, Y. Liu, S. Rangan, and E. Erkip, "Millimeter wave picocellular system evaluation for urban deployments," in *Proc. IEEE Globecom Workshops (GC Wkshps)*, Dec. 2013, pp. 105–110.

[5] S. Rangan, T. S. Rappaport, and E. Erkip, "Millimeter-wave cellular wireless networks: Potentials and challenges," *Proc. IEEE*, vol. 102, no. 3, pp. 366–385, Mar. 2014.

[6] Z. Zhang, J. Ryu, S. Subramanian, and A. Sampath, "Coverage and channel characteristics of millimeter wave band using ray tracing," in *Proc. IEEE Int. Conf. Commun. (ICC)*, Jun. 2015, pp. 1380–1385.

[7] M. R. Akdeniz *et al.*, "Millimeter wave channel modeling and cellular capacity evaluation," *IEEE J. Sel. Areas Commun.*, vol. 32, no. 6, pp. 1164–1179, Jun. 2014.

[8] H. Zhao *et al.*, "28 GHz millimeter wave cellular communication measurements for reflection and penetration loss in and around buildings in New York city," in *Proc. IEEE Int. Conf. Commun. (ICC)*, Jun. 2013, pp. 5163–5167.

[9] J.-H. Jung, J. Lee, J.-H. Lee, Y.-H. Kim, and S.-C. Kim, "Ray-tracing-aided modeling of user-shadowing effects in indoor wireless channels," *IEEE Trans. Antennas Propag.*, vol. 62, no. 6, pp. 3412–3416, Jun. 2014.

[10] J. W. McKown and R. L. Hamilton, Jr., "Ray tracing as a design tool for radio networks," *IEEE Netw.*, vol. 5, no. 6, pp. 27–30, Nov. 1991.

[11] K. Rizk, J.-F. Wagen, and F. Gardiol, "Two-dimensional ray-tracing modeling for propagation prediction in microcellular environments," *IEEE Trans. Veh. Technol.*, vol. 46, no. 2, pp. 508–518, May 1997.

[12] Y. Chang, S. Baek, S. Hur, Y. Mok, and Y. Lee, "A novel dual-slope mm-Wave channel model based on 3D ray-tracing in urban environments," in *Proc. IEEE 25th Annu. Int. Symp. Pers., Indoor, Mobile Radio Commun. (PIMRC)*, Sep. 2014, pp. 222–226.

[13] S. Hur *et al.*, "28 GHz channel modeling using 3D ray-tracing in urban environments," in *Proc. IEEE 9th Eur. Conf. Antennas Propag. (EuCAP)*, Apr. 2015, pp. 1–5.

[14] G. Liang and H. L. Bertoni, "A new approach to 3-D ray tracing for propagation prediction in cities," *IEEE Trans. Antennas Propag.*, vol. 46, no. 6, pp. 853–863, Jun. 1998.

[15] H. Fuchs, Z. M. Kedem, and B. F. Naylor, "On visible surface generation by *a priori* tree structures," *ACM Siggraph Comput. Graph.*, vol. 14, no. 3, pp. 124–133, 1980.

[16] T. S. Rappaport *et al.*, *Wireless Communications: Principles and Practice*, vol. 2. Englewood Cliffs, NJ, USA: Prentice-Hall, 1996.

[17] D. Ferreira, I. Cuiñas, R. F. S. Caldeirinha, and T. R. Fernandes, "A review on the electromagnetic characterisation of building materials at micro- and millimetre wave frequencies," in *Proc. 8th Eur. Conf. Antennas Propag. (EuCAP)*, Apr. 2014, pp. 145–149.

[18] S. Hur *et al.*, "Proposal on millimeter-wave channel modeling for 5G cellular system," *IEEE J. Sel. Topics Signal Process.*, vol. 10, no. 3, pp. 454–469, Apr. 2016.

[19] J.-J. Park, J. Liang, J. Lee, H.-K. Kwon, M.-D. Kim, and B. Park, "Millimeter-wave channel model parameters for urban microcellular environment based on 28 and 38 GHz measurements," in *Proc. IEEE 27th Annu. Int. Symp. Pers., Indoor, Mobile Radio Commun. (PIMRC)*, Sep. 2016, pp. 1–5.

[20] J.-H. Lee, J.-S. Choi, J.-Y. Lee, and S.-C. Kim, "Permittivity effect of building materials on 28 GHz mmWave channel using 3D ray tracing simulation," in *Proc. IEEE Global Commun. Conf. GLOBECOM*, Dec. 2017, pp. 1–6.

[21] R. J. Luebbers, "Finite conductivity uniform GTD versus knife edge diffraction in prediction of propagation path loss," *IEEE Trans. Antennas Propag.*, vol. AP-32, no. 1, pp. 70–76, Jan. 1984.

[22] R. G. Kouyoumjian and P. H. Pathak, "A uniform geometrical theory of diffraction for an edge in a perfectly conducting surface," *Proc. IEEE*, vol. 62, no. 11, pp. 1448–1461, Nov. 1974.

[23] J. B. Keller, "Geometrical theory of diffraction," *J. Opt. Soc. Amer.*, vol. 52, no. 2, pp. 116–130, 1962.

[24] P. A. Tenerelli and C. W. Bostian, "Measurements of 28 GHz diffraction loss by building corners," in *Proc. 9th IEEE Int. Symp. Pers., Indoor Mobile Radio Commun.*, vol. 3. Sep. 1998, pp. 1166–1169.

[25] J. Lee, J. Liang, M.-D. Kim, J.-J. Park, B. Park, and H. K. Chung, "Measurement-based propagation channel characteristics for millimeter-wave 5G Giga communication systems," *ETRI J.*, vol. 38, no. 6, pp. 1031–1041, 2016.

[26] T. S. Rappaport, G. R. Maccartney, M. K. Samimi, and S. Sun, "Wideband millimeter-wave propagation measurements and channel models for future wireless communication system design," *IEEE Trans. Commun.*, vol. 63, no. 9, pp. 3029–3056, Sep. 2015.

[27] S. Nie, G. R. MacCartney, S. Sun, and T. S. Rappaport, "28 GHz and 73 GHz signal outage study for millimeter wave cellular and backhaul communications," in *Proc. IEEE Int. Conf. Commun. (ICC)*, Jun. 2014, pp. 4856–4861.

[28] J. G. Andrews *et al.*, "What will 5G be?" *IEEE J. Sel. Areas Commun.*, vol. 32, no. 6, pp. 1065–1082, Jun. 2014.

[29] W. Roh *et al.*, "Millimeter-wave beamforming as an enabling technology for 5G cellular communications: Theoretical feasibility and prototype results," *IEEE Commun. Mag.*, vol. 52, no. 2, pp. 106–113, Feb. 2014.

[30] S. Sesia, I. Toufik, and M. Baker, *LTE—The UMTS Long Term Evolution*. New York, NY, USA: Wiley, 2009.

Jae-Hyun Lee received the B.S. degree in electrical engineering from the Pohang University of Science and Technology, Pohang, South Korea, in 2012, and the joint M.S. and Ph.D. degrees in electrical engineering from Seoul National University, Seoul, South Korea, in 2018.

His current research interests include wireless propagation channel measurement & modeling, ad-hoc networks, machine learning, millimeter wave communication, and the ray-tracing simulation of wireless networks.

Jeong-Sik Choi received the B.S. degree in electrical engineering from the Pohang University of Science and Technology, Pohang, South Korea, in 2010, and the M.S. and Ph.D. degrees in electrical engineering from Seoul National University, Seoul, South Korea, in 2012 and 2016, respectively.

From 2016 to 2017, he was a Senior Researcher with the Institute of New Media and Communications, Seoul National University, Seoul. He is currently a Post-Doctoral Researcher at Intel Labs, Intel Corporation, Santa Clara, CA, USA. His current research interests include wireless propagation channel measurement & modeling, wireless resource management, and the application of machine learning algorithms for indoor and outdoor positioning techniques.

Seong-Cheol Kim (S'91–M'96–SM'12) received the B.S. and M.S. degrees in electrical engineering from Seoul National University, Seoul, South Korea, in 1984 and 1987, respectively, and the Ph.D. degree in electrical engineering from the Polytechnic Institute of New York University, Brooklyn, NY, USA, in 1995.

From 1995 to 1999, he was with the Wireless Communications Systems Engineering Department, AT&T Bell Laboratories, Holmdel, NJ, USA. Since 1999, he has been a Professor with the Department of Electrical Engineering and Computer Science, Seoul National University. His current research interests include the systems engineering of wireless communication, including propagation channel modeling, localization, and resource management, power-line communication, and automotive radar system.